Shap. Mem. Superelasticity (2023) 9:35–49
https://doi.org/10.1007/s40830-023-00422-4

TECHNICAL ARTICLE

Thin-Film Superelastic Alloys for Stretchable Electronics

Sabrina M. Curtis[1,2] · Jascha L. Gugat[3] · Lars Bumke[1] · Duygu Dengiz[1] · Lena Seigner[4] · Don Schmadel[5] · Nathan S. Lazarus[6] · Eckhard Quandt[1]

Received: 10 September 2022 / Revised: 9 December 2022 / Accepted: 23 January 2023 / Published online: 1 March 2023

Abstract Conductive serpentine interconnects comprise fundamental building blocks (e.g., electrodes, antennas, wires) of many stretchable electronic systems. Here we present the first numerical and experimental studies of freestanding thin-film TiNiCuCo superelastic alloys for stretchable interconnects. The electrical resistivity of the austenite phase of a $Ti_{53.3}Ni_{30.9}Cu_{12.9}Co_{2.9}$ thin-film at room temperature was measured to be 5.43×10^{-7} Ω m, which is larger than reported measurements for copper thin-films (1.87×10^{-8} Ω m). Structuring the superelastic conductor to limit localized strain using a serpentine geometry led to freestanding interconnects that could reach maximum serpentine elongations of up to 153%. Finite element analysis (FEA) simulations predicted that superelastic serpentine interconnects can achieve significantly larger (~5X–7X) elastic elongations than copper for the same serpentine geometry. FEA predictions for stress distribution along the TiNiCuCo serpentine interconnect were experimentally verified by infrared imaging and tensile testing experiments. The superior mechanical advantages of TiNiCuCo were paired with the high electronic conductivity of copper, to create Cu/TiNiCuCo/Cu serpentine composites that were demonstrated to serve as freestanding electrical interconnects between two LEDs. The results presented in this manuscript demonstrate that thin-film superelastic alloys are a promising material class to improve the performance of conductors in stretchable and flexible electronics.

Keywords Mechanical behaviors · Shape memory films · Superelasticity · Stress-induced martensitic phase transformations

This article is an invited submission to *Shape Memory and Superelasticity* selected from presentations at the Shape Memory and Superelastic Technology Conference and Exposition (SMST2022) held May 16–20, 2022 at The Westin Carlsbad Resort, San Diego, California, and has been expanded from the original presentation. The issue was organized by Dr. Srinidhi Nagaraja, G.RAU, Inc. and Dr. Ashley Bucsek, University of Michigan.

✉ Sabrina M. Curtis
sabrina@khanjur.com

[1] Inorganic Functional Materials, Faculty of Engineering, Kiel University, Kiel, Germany

[2] Department of Materials Science and Engineering, University of Maryland, College Park, MD, USA

[3] Acquandas GmbH, Kiel, Germany

[4] Institute of Microstructure Technology, Karlsruhe Institute of Technology, Karlsruhe, Germany

[5] Institute for Research in Electronics & Applied Physics, University of Maryland, College Park, MD, USA

[6] Electrical and Computer Engineering Department, University of Delaware, Newark, DE, USA

Introduction

The next-generation of biointegrated devices [1], epidermal electronics [2], and wearable energy harvesting and storage devices [3] must accommodate large levels of physical deformation (i.e., elastic strains as large as 75–100%) [4, 5] to ensure conformal contact to the human skin and tissue. Flexible and stretchable electronics use microelectromechanical systems (MEMS)-inspired techniques to reconfigure thin-film electronic components into new designs that can withstand high levels of flexing, bending, and twisting deformation [6–8]. As depicted in the schematic in Fig. 1a, the popular "island plus serpentine" design connects functional device "islands" by wavy serpentine

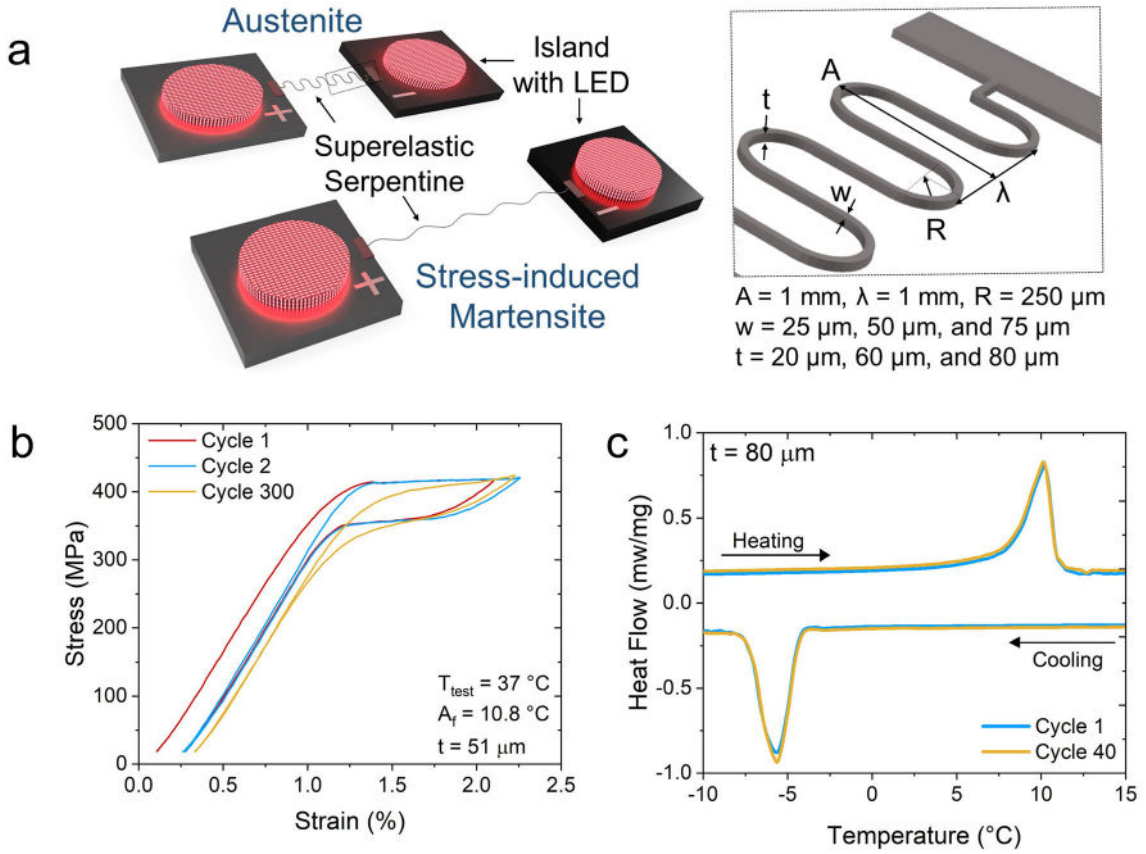

Fig. 1 **a** 3D schematic demonstrating "island plus serpentine" stretchable design with a superelastic serpentine interconnect at equilibrium in the austenite phase and stretched in the stress-induced martensite phase. (insert) Serpentine geometry dimensions investigated in this study. **b** Tensile testing curves of a 51 μm thick TiNiCuCo dogbone specimen after superelastic cycling between $\varepsilon = 0$ and 2.1% for 300 cycles. **c** Differential scanning calorimetry curves demonstrating thermal reversibility for an 80 μm thick TiNiCuCo sample for 40 cycles.

interconnects. Under an applied force, the serpentine will elongate by changing shape to accommodate the deformation of the stretchable circuit. The serpentine structure non-uniformly distributes stress/strain throughout the geometry, enabling the serpentine to elastically elongate to large levels of applied strains [9–11]. At the same time, under deformation, the islands undergo low stresses, enabling them to house any stress-sensitive components (e.g., photovoltaics, batteries, LEDs, or embedded sensor elements) [3, 8, 12]. Essentially, the serpentine structure can enable any material to become stretchable including, for example, liquid metal [13], thin-film metals such as copper (Cu) [12, 14–17] and gold [3], and semiconductors such as silicon [18–21] and gallium nitride [22, 23].

Nickel-titanium (NiTi) is one of the most commercially prevalent shape memory alloys (SMAs) because of its large reversible transformation strain of up to $\varepsilon = 8\%$ [24, 25]. Sputtered thin-film NiTi-alloys are employed in numerous high-bending applications such as self-expanding stents [26], micro-valves [27, 28], micro-actuators [28–31], and other types of microdevices [32, 33]. Additionally, it has been shown that thin-film NiTi stents can be functionalized with other materials such as Pt or PtIr electrodes for bioelectronic sensing to produce next-generation smart medical devices [26]. The strain recovery of up to $\varepsilon = 8\%$ in NiTi-alloys is enabled by a reversible structural phase transformation between monoclinic (B19') or orthorhombic (B19) martensite and cubic (B2) austenite [34]. Through a twinning/detwinning process, martensite can be deformed to extremely large strains which can be entirely recovered by a thermally induced phase transformation, known as the *shape memory effect*. In the case of austenite, large superelastic strains are recovered through a stress-induced phase transformation from austenite to stress-induced martensite, known as, the *superelastic effect* [25]. With proper chemical composition, fabrication (e.g., multilayer sputter deposition approach) [35], heat treatment, and surface finish, thin-film SMAs like $Ti_{54}Ni_{34}Cu_{12}$ and $Ti_{54.7}Ni_{30.7}Cu_{12.3}Co_{2.3}$ can repeatedly undergo this transformation with ultralow-fatigue [36]. These thin-film SMAs were shown to undergo the superelastic transformation to a strain of $\varepsilon = 2\%$ for 10+ million cycles

[35, 36]. Despite other known advantageous properties of NiTi SMAs such as bio-compatibility, corrosion resistance [24], high strength, high actuation densities, and good electrical conductivity [25], these SMAs are seldom employed in stretchable electronic applications [37].

Recently, the superior mechanical properties offered by superelastic NiTi wires were shown to be advantageous compared to Cu wires for stretchable electronics. 100 μm thick serpentine structures of superelastic NiTi wires were shown to have a high elastic stretchability of 196% credited to the large intrinsic superelastic strains of ε = 7.5% achievable by NiTi, as well as the non-uniform strain distribution offered by the serpentine structure [37]. These NiTi serpentine wires were demonstrated to reversibly cycle stretching of 100% for 1000 cycles, whereas Cu wire serpentine interconnects were plastically deformed after stretching to 100% for one cycle [37]. Cu is currently the most widely used stretchable conductor due to its very low electrical resistivity 1.87×10^{-8} Ω m [38]. The electrical resistivity of liquid metal EGaIn, another popular conductor used in stretchable electronics, is 1.77×10^{-6} Ω m [39]. In comparison, NiTi is reported to have an electrical resistivity of 7.6×10^{-7} Ω m in the martensite phase, and 1.0×10^{-6} Ω m in the austenite phase [25]. While Cu thin-films have superior electrical properties compared to SMAs, the challenge with stretchable Cu interconnects is their low intrinsic elastic strain (ε = 0.26% [40]) which leads to the accumulation of plastic deformation in the interconnect at low applied serpentine elongations.

The experimental and numerical studies presented here compare the mechanical and electrical properties of thin-film superelastic TiNiCuCo serpentine interconnects with thin-film Cu serpentine interconnects for use in stretchable electronic applications. Following a MEMS-compatible fabrication process developed by *Lima de Miranda* [41, 42], one can fabricate freestanding SMA thin-films into any custom stretchable geometry (e.g. auxetic geometries [43]) with feature sizes as small as 10 microns. The stress-induced phase transformation from austenite to stress-induced martensite can be used to develop stretchable circuits that can reversibly stretch to large levels of applied external strain, as depicted in Fig. 1a. Thermal-mechanical behavior of the TiNiCuCo serpentines are evaluated by comparing direct experimental results with finite element analysis simulations.

Additionally, the results presented in this work demonstrate that Cu/SMA composites can combine the excellent electrical conductivity of Cu thin-films with the superior mechanical properties of superelastic thin-films to develop freestanding stretchable interconnects that are both conductive and reversibly stretchable. While we demonstrate only one composition of a TiNiCuCo alloy, our results show the promise of integrating various other thin-film NiTi-based SMAs into stretchable electronics.

Experimental

Sample Preparation

Free-standing SMA films were fabricated through a combination of UV-lithography, DC magnetron sputtering, and a wet chemical etching process as described in detail by Lima de Miranda et al. [41]. The films included single-period and five-period serpentine mechanical test structures with three different thicknesses (t = 20 μm, 60 μm, and 80 μm) and serpentine widths (w = 25 μm, 50 μm, and 75 μm). As shown in the insert in Fig. 1a, all fabricated serpentines had an arc radius (R) = 250 μm, a wavelength (λ) = 1 mm, and a peak-to-peak amplitude (A) = 1 mm. A cluster magnetron sputtering device with a base pressure $< 3\times10^{-7}$ mbar (model CS730S by Von Aardenne GmbH, Germany) was used to sputter amorphous TiNiCuCo onto a pre-structured 100 mm silicon substrate. Sputtering took place with a 200 mm TiNiCuCo target (FHR Anlagenbau GmbH, Germany) at a pressure of 2×10^{-3} mbar, an argon flow of 20 sccm, and a DC power of 300W, resulting in a deposition rate of ~2 μm / hour. Rapid thermal annealing (RTA) using an RTA-6 SY09 (Createc Fischer, Germany, base pressure $< 1\times10^{-7}$ mbar) was performed at 700 °C for 15 minutes with a heating rate of 50 °C /s to crystallize the amorphous films. Due to slight variations in the fabrication process, the cross-section of the serpentine's area varies by up to 10% and exhibits a trapezoidal cross-sectional shape rather than the desired rectangle cross-section. Additionally, thickness variations of up to 10% were found from the center to the edge of the wafer. These compositional and geometrical variations are expected sources of error in the following measurements and experiments.

Energy Dispersive X-ray Spectroscopy (EDX)

The actual film composition of a 5 μm thick amorphous TiNiCuCo layer on a 100 mm Si substrate was determined using a Helios NanoLab 600 scanning electron microscopy (FEI, Germany) equipped with energy-dispersive X-ray spectroscopy (EDX) silicon drift detector (Oxford Instruments, UK). Quantitative analysis used a $Ti_{49.60}Ni_{50.40}$ binary standard. EDX measurements were taken in a line scan across the sputtered amorphous TiNiCuCo film on a 100 mm silicon substrate. The composition was found to vary from $Ti_{53.3}Ni_{30.9}Cu_{12.9}Co_{2.9}$ at the center and $Ti_{53.0}Ni_{31.5}Cu_{12.7}Co_{2.8}$ at the edge of the wafer, with an error around ± 0.5 at %. This characterization wafer is in

addition to the freestanding wafers with serpentine specimens.

Differential Scanning Calorimetry (DSC)

Thermal analysis included thermal cycling of all fabricated TiNiCuCo films and was conducted on a differential scanning calorimeter (DSC 204 F1 Phoenix by Netzsch, Germany). The heating and cooling rate was 10 °C min^{-1}. The transformation temperatures and latent heat of the SMA were determined using the internal software, Proteus 7.1.0, and the tangent method. Thermal hysteresis was calculated according to $\Delta T = \frac{1}{2}\left(A_s + A_f - M_s - M_f\right)$, where A_s and A_f corresponds to the austenite start and finish temperatures, and M_s and M_f correspond to the martensite start and finish temperature.

Tensile Testing

Functional stability of the phase transformation during superelastic mechanical cycling of a TiNiCuCo dogbone specimen and single-period serpentines was evaluated using a tensile tester (Zwick Roell Z.05) at a temperature of 37 °C using a strain rate frequency of 0.02 Hz to maintain isothermal loading conditions. The dogbone specimen was preloaded to a force of 0.5 N prior to measurement, whereas serpentine specimens were preloaded by a much smaller force of 0.001 N. Figure 1b demonstrates the superelastic hysteresis loop of a TiNiCuCo dogbone specimen (parallel length of 13 mm, 500 µm wide, 51 µm thick). After 300 cycles between ε = 0–2.1% there was unrecoverable plastic strain ($\varepsilon_{plastic}$ = 0.28%), due to the buildup of remnant martensite.

Due to the non-uniform cross-section across the serpentine mechanical test structures, the data are reported as 'force vs serpentine elongation' instead of 'stress vs strain'. Serpentine elongation is defined as $\frac{\Delta l}{l}$*100% where l is the initial end-to-end length of the serpentine in the equilibrium position when the sample is in the austenite phase under no applied external force. Tensile testing took place on single-period serpentine mechanical test structures, with an initial end-to-end length, i.e., the end-to-end distance, l = 1 mm.

Electrical Resistivity of TiNiCuCo

The electrical resistivity of an 18.6 µm thick TiNiCuCo film was determined using four-point resistance measurements carried out inside a cryostat. Quasi-stationary conditions help guarantee that the temperature is constant so that thermally induced changes in resistance are negligible during measurement. The electrical resistivity of the austenite phases at room temperature of TiNiCuCo was determined to be 5.43×10^{-7} Ω m, slightly lower than the resistivity reported for binary NiTi [25].

Stress-Induced Electrical Properties

The stress-dependent electrical properties were determined for 20 µm thick five-period serpentine mechanical test structures having 5 mm unstretched length using a custom-built translation stage to allow four-point resistance measurements while stretching the serpentine. Serpentines were loaded and unloaded at room temperature at a rate of 0.5 mm/s for serpentine elongations of 0–30% for 1000 cycles. A power supply provided a constant current of 0.05 A ± 0.005 A along the serpentine trace, while an ohmmeter monitored the change in electrical resistance.

Stretchable LED Demonstration

Here we consider metallic thin-film superelastic serpentines as freestanding substrates for other conductors for use in stretchable electronics. Cu/TiNiCuCo/Cu serpentine composites were used as freestanding electrical interconnects between two LEDs. The wettability of solder on SMA surfaces is known to be poor because the surface of NiTi-based SMAs forms a stable native oxide layer (TiO_2). However, the thin layer of sputtered copper or gold on top of the native TiO_2 layer on TiNiCuCo films was found to make a stable connection for lead-based solder. TiNiCuCo five-period serpentines with t/w = 20/75 and 80/75 were sputter-deposited with 5 µm thick Cu on one side, and 500 nm Cu on the other side. Each Cu/TiNiCuCo/Cu serpentine composite was then soldered between two red LEDs (Lumitronix LED-Technik GmbH, Germany). A copper wire (diameter = 0.5 mm) was soldered between the external LED contact pads and connected to a power supply. A constant voltage (V) of 3.5 V was applied to the circuit. The current (I) and corresponding resistance (R) was monitored as a function of serpentine elongation. The resistance of the circuit is calculated according to ohms law (R = I/V). Potential mechanical inconsistencies in the experimental set-up such as solder joint integrity, wire lengths, and power supply fluctuations are sources of error in this experiment. Another source of error that is not considered is local temperature fluctuations that arise from the latent heat of transformation upon stretching superelastic materials [44].

Infrared (IR) Thermography

Single-period and five-period serpentine mechanical test structures (t = 60 µm, w = 50 µm) were spray-coated with a ~10 µm carbon coating (Graphit33, CRC Industries).

Single-period serpentines were loaded and unloaded at room temperature at a strain rate of 20 mm/s between serpentine elongations of 0–33%. Five-period serpentines were tested with a strain rate of 15 mm/s. A FLIR A655sc camera with a minimum pixel size of 11 µm was used to detect changes in the temperature at regions of maximum strain concentration in the serpentine.

Results

Thermal-Induced Martensitic Transformation

The most practical SMAs for stretchable systems will be those that have austenite finish temperatures (A_f) below room temperature, to ensure all applied deformation to the stretchable SMA can be recovered through the superelastic effect. Differential scanning calorimetry (DSC) was used to evaluate the martensitic transformation temperatures and enthalpies from TiNiCuCo samples with different thicknesses (t = 20 µm, 60 µm, 80 µm) and prepared in different wafer batches. As shown in Table 1 all samples have austenite finish (A_f) temperatures between 10 °C and 11 °C, therefore they are superelastic at room temperature. Similar transition temperatures and latent heat values were obtained for all samples which indicates that all samples have similar atomic compositions and microstructure characteristics. DSC was also used to evaluate thermal fatigue in all samples. Figure 1c demonstrates good thermal reversibility for an 80 µm thick TiNiCuCo film. After 40 cycles, there was a change of less than 0.1K and 0.1 J/g in the martensitic/ austenitic transformation temperatures and transformation enthalpies, respectively, implying that all fabricated samples have low functional fatigue [45]. Additionally, all fabricated samples have a narrow thermal hysteresis (ΔT = 14 °C–15.5 °C), which indicates that the middle eigenvalue of transformation strain is close to zero which is a prerequisite for cycling stability [46, 47].

In some cases, upon cooling, a double peak was observed on the martensite peak for the 20 and 60 µm thick samples which might be an indication that an intermediate phase transition occurs during the phase transformation. Alternatively, the double peaks could arise due to the inhomogeneity of the microstructure throughout the sample [48, 49]. To precisely determine the origin of the multi-step transformation and one must confirm the size and homogeneity of the Ti_2Cu precipitates using temperature-dependent X-ray diffraction, transmission electron microscopy, and scanning electron microscopy studies. Such experiments are beyond the scope of this work. The reader is guided to the following studies on the influence of microstructure, and crystallographic phase compatibility on the functional and structural fatigue of thin-film SMAs [35, 45–47].

Superelastic Serpentine Mechanics

The maximum elongation achieved by a serpentine is dependent on the material's mechanical properties, as well as the dimensions of the serpentine's thickness/width (t/w) aspect ratio. Su et al. showed the scissoring or buckling mechanical deformation mode of a serpentine trace is dependent on the t/w aspect ratio of the serpentine geometry [40]. Buckling deformation occurs when the t/w < 1, because rotational and torsional forces cause the serpentine to bend and twist out-of-plane [12]. Scissoring occurs when the t/w > 1, because rotation is no longer feasible, and therefore only in-plane (non-buckling) deformation is possible [40].

The maximum serpentine elongation at fracture along with the geometrical buckling/scissoring dependence was determined through strain-to-rupture tests on five-period serpentine mechanical test structures. All samples were mounted in a custom-built 3D-printed holder which could precisely apply a uniaxial displacement to the fabricated serpentine structures while taking optical images. Serpentine elongation ($\frac{\Delta l}{l}$*100%, where l = 5 mm) was calculated

Table 1 Martensitic transformation temperatures and enthalpy of transformation obtained from the center of the wafer for cycle 1 and cycle 40 on fabricated 20 µm, 60 µm, and 80 µm thick films, determined by DSC.

TiNiCuCo film thickness	Cycle number	A_s [°C]	A_f [°C]	A_p [°C]	$\Delta H_{M\rightarrow A}$ [J/g]	M_s [°C]	M_f [°C]	M_p [°C]	$\Delta H_{A\rightarrow M}$ [J/g]	ΔT [°C]
20 µm	Cycle 1	8.62	9.96	9.36	7.22	− 4.63	− 5.59	− 5.10	9.95	14.40
20 µm	Cycle 40	8.62	9.91	9.36	7.14	− 4.63	− 5.57	− 5.09	10.04	14.37
60 µm	Cycle 1	9.29	11.01	10.39	7.10	− 3.84	− 5.18	− 4.62	10.18	14.66
60 µm	Cycle 40	9.31	11.01	10.39	7.08	− 3.84	− 5.23	− 4.63	10.24	14.70
80 µm	Cycle 1	8.46	11.00	10.26	6.98	− 4.34	− 7.30	− 5.66	9.48	15.55
80 µm	Cycle 40	8.34	10.93	10.14	7.09	− 4.33	− 7.20	− 5.63	9.37	15.40

through image processing with the program Image J. Figure 2a shows the average maximum applied serpentine elongation before fracture as a function of the t/w aspect ratio. Where provided, the error bars represent the standard deviation from the average value of each measurement for at least three tested serpentine samples. Serpentines of all t/w ratios were found to reach large maximum serpentine elongations between 72 and 153%. As the serpentine width or thickness increases, the effective stiffness of the cross-section becomes greater, thus smaller uniaxial displacements result.

Freestanding SMA serpentines are found to follow similar buckling and scissoring deformation dependencies reported for thin-film Cu serpentines [40]. When the serpentine thickness was increased to 80 µm, only in-plane bending, i.e., scissoring, deformation is obtained. Figure 2b shows scissoring deformation behavior for superelastic serpentines with t/w = 60/25, 80/25, and 80/75. The serpentine samples are unstretched in the austenite phase at equilibrium. The phase transformation to stress-induced martensite occurs by stretching the serpentine. Samples with a serpentine width of 25 µm (t/w = 20/25, 60/25, and 80/25) exhibited average maximum serpentine elongations of 153% ± 4%, approaching the shape of a straight line, with kinks. As shown in Fig. 2c, all 20 µm thick serpentines have a t/w < 1, and in these cases, the serpentines deflect out-of-plane under elongation, resulting in buckling deformation. All 20 µm thick samples (t/w = 20/25, 20/50, and 20/75) were found to reach maximum applied elongations between 135 and 153%. After sample fracture, all tested serpentine segments, regardless of serpentine thickness or width, mostly returned to their equilibrium form with only minimal observable plastic strain, as shown in Fig. 2c. Only slight plastic deformation was observed at the regions of maximum stress, which includes the anchor connection points of the mechanical frame, as well as in the curved regions of the serpentine structure (i.e., arc). Plastic strain accumulation in the superelastic interconnect could be mitigated using a stretchable geometry that distributes stress more uniformly throughout the structure (e.g., fractal serpentine interconnects [20], archimedean spirals [50], stretchable auxetic geometries [43]).

Finite Element Analysis and Experimental Comparison

The performance of superelastic TiNiCuCo serpentine and Cu serpentine interconnects under strain loading conditions are numerically compared utilizing finite element analysis (FEA). Gugat et al. [51] previously developed a custom 2D FEA model using COMSOL Multiphysics 5.3a to evaluate the thermal-mechanical behavior of structured NiTi thin-films under strain loading. This model was adapted to analyze and compare the stretchable behavior of TiNiCuCo and Cu serpentines. The model includes SMA dynamic mechanical analysis and kinetic energy transfer simulations to allow the simultaneous analysis of the von Mises stress distribution, maximum principal strains, and the volume

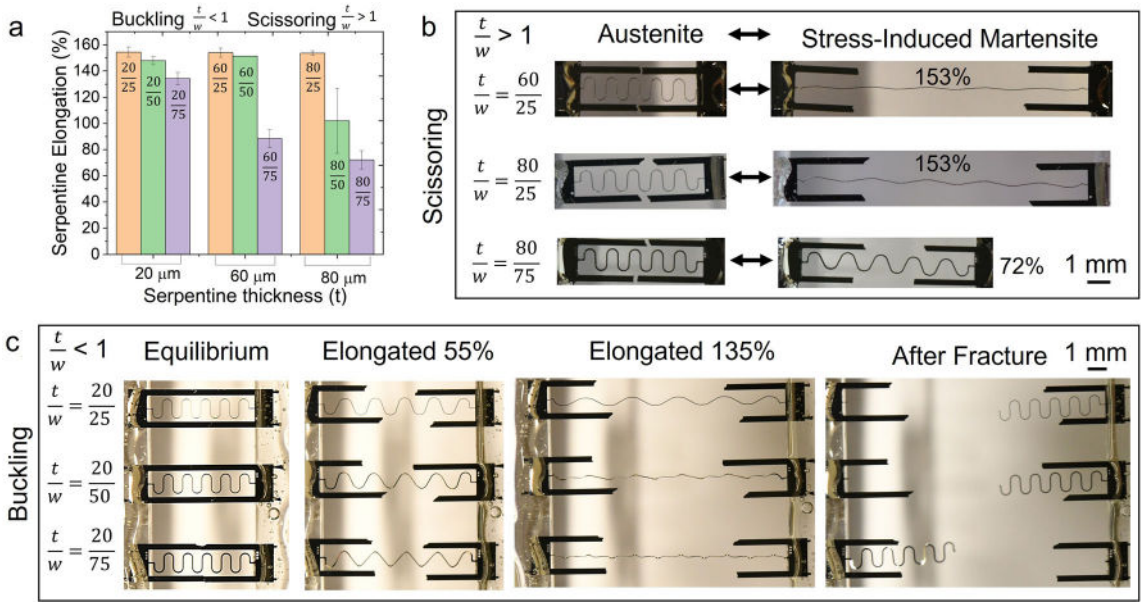

Fig. 2 Buckling and scissoring deformation dependence for superelastic serpentines. **a** Maximum serpentine elongation at fracture for all tested serpentine specimens. **b** Demonstration of scissoring deformation (t/w > 1) for serpentines with t/w = 60/25, 80/25 and 80/75. **c** Demonstration of buckling deformation (t/w < 1) for serpentines with t/w = 20/25, 20/50, and 20/75. The fracture images show superelastic recovery after applying the maximum serpentine elongation to the specimens.

fraction of material that transformed from austenite to stress-induced martensite.

The SMA material properties (critical stress, critical strain, transformation temperatures, and Clasius-Claperyon coefficients (C_{AM}, C_{MA})) of TiNiCuCo for the FEA model were estimated based on the results of temperature-dependent tensile testing and differential calorimetry experiments. Figure 3 demonstrates temperature-dependent tensile tests at 37, 55, and 65 °C on a fabricated free-standing TiNiCuCo dog bone specimen (parallel length of 13 mm, 500 µm wide, 51 µm thick). Experimental tensile testing results were empirically fit to extract several of the material properties used in the model, see Table 2**.** The comparison of the experiment and FEA results determined the recoverable strain from the superelastic transformation for TiNiCuCo to be $\varepsilon = 1.8\%$. There was a total of $\varepsilon_{plastic} = 0.28\%$ in the sample because the dogbone had previously been cycled between $\varepsilon = 0$–2.1% for 300 cycles, as is shown in Fig. 1a. The influence of fatigue and plastic deformation is not implemented into the SMA model. For simulations, the yield stress and elastic strain limit for Cu were determined to be 200 MPa, and 0.26%, respectively. The Cu material properties are similar to the properties reported in theoretical and experimental studies of buckling and scissoring thin-film Cu serpentine interconnects on polymer substrates [40]. A summary of the most important material properties considered in the simulation is given in Table 2**,** however, the full list of all parameters used in the model is given by Gugat et al. [51].

Structural mechanical FEA simulations were implemented for 2D problems with plane stress assumptions,

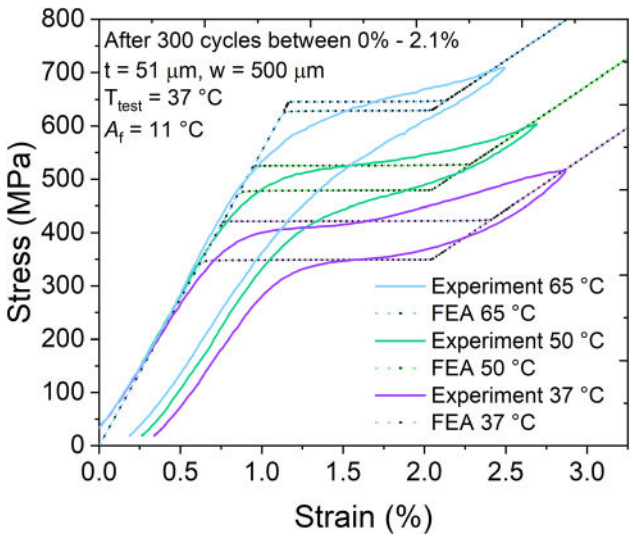

Fig. 3 Temperature-dependent tensile test performed on traditional TiNiCuCo dogbone. Experimental tensile testing results were empirically fit to extract several of the FEA parameters (e.g., Clasius-Claperyon Coefficient). Dotted curves show FEA results while solid curves show the experiment

neglecting possible out-of-plane movement. Therefore, the simulations are more accurate for thicker serpentines (e.g., $t = 60$ µm and 80 µm) that were shown to deform in-plane through scissoring deformation. The stretching performance of single-period Cu and TiNiCuCo serpentines are numerically compared by FEA for 80 µm thick serpentines with varying widths (t/w = 80/10–80/80). The maximum quasi-elastic serpentine elongation for a superelastic material is determined by the recoverable strain of the superelastic phase transformation. Simulations are performed by holding one end of the serpentine fixed and applying a uniaxial displacement until the maximum principal strain (or von Mises stress) in the serpentine exceeds the elastic stress or strain limit of materials. Figure 4a shows the FEA prediction of the maximum elastic serpentine deformation as a function of serpentine width for 80 µm thick TiNiCuCo and Cu. These simulation results predict that the maximum quasi-elastic serpentine elongation for TiNiCuCo is at least ∼5X–7X larger than Cu, depending on the t/w ratio of the geometry. Through FEA, it was determined that the fracture stress for Cu thin-films was between 607 and 715 MPa at intrinsic strains of $\varepsilon = 0.54$–0.64 %. As shown in Fig. 4b FEA predicts that a Cu serpentine with a t/w = 80/25 would be fractured at serpentine elongations of 13% whereas a TiNiCuCo of the same dimensions could elastically elongate to 32%. TiNiCuCo serpentines with t/w = 80/25 were found to experimentally fracture at serpentine elongations of 153%. Simulation results predict that the serpentine structure will accumulate strain in localized regions (e.g., inner arcs) when deforming in-plane through scissoring deformation. The greater ductility offered by superelastic materials also allows superelastic interconnects to reach much larger levels of applied external strain before fracture compared to Cu interconnects.

The model was also able to closely predict the superelastic hysteresis loop shape and maximum critical forces for serpentines of all t/w aspect ratios. For example, Fig. 4c shows the superelastic hysteresis loop between the experiment and FEA model for a TiNiCuCo serpentine (t/w = 60/75) when elongated between 0 and 50%. FEA results of Cu in the same constitute geometry are also plotted in Fig. 4c to demonstrate that a Cu serpentine undergoes much larger forces at lower applied serpentine strains compared to TiNiCuCo. Additionally, the 60 µm TiNiCuCo sample experimentally did not superelastically complete the phase transformation, reflected by the 4.8% plastic serpentine elongation caused by remnant martensite after one cycle. The formation of plastic strain implies that the maximum principal strain in the TiNiCuCo likely exceeded $\varepsilon = 1.8\%$. Figure 4d shows that when a serpentine with t/w = 20/75 is elongated to 50%, its phase transformation was entirely recovered through the superelastic

Table 2 Material parameters of copper and TiNiCuCo thin-films used in FEA simulations.

	Density [kg/m^3]	Poisson's ratio	Young's modulus [GPa]	Elastic strain limit (ε):	Transformation temperature [°C]	Clasius-Claperyon coefficient [MPa/K]
Copper	8940	0.34	119	0.26%	NA	NA
TiNiCuCo (martensite)	6450	0.33	20	1.8%	$M_s = -10$ °C $M_f = -53.09$ °C	$C_{AM} = 8.0$
TiNiCuCo (austenite)	6450	0.33	55	1.8%	$A_s = 0$ °C $A_f = 5$ °C	$C_{MA} = 10.0$

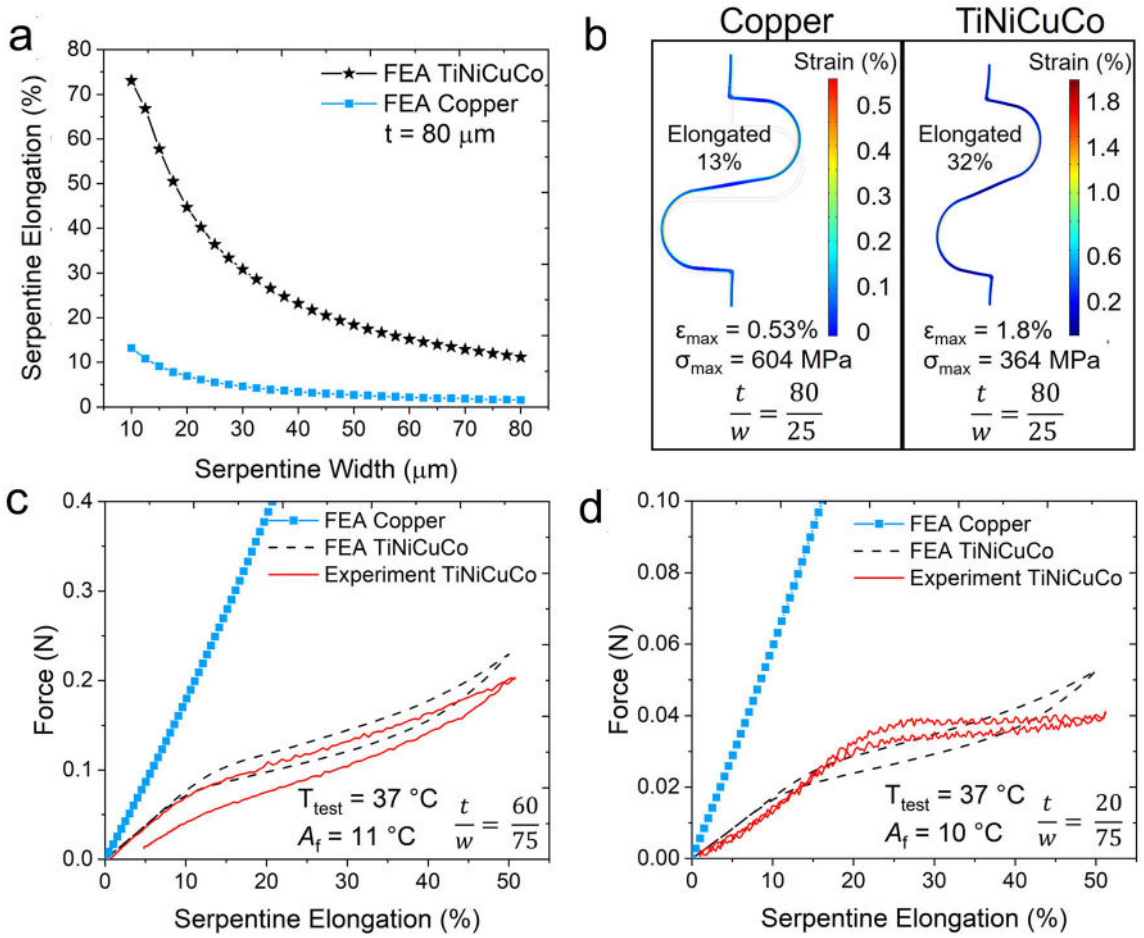

Fig. 4 **a** FEA comparison of maximum elastic serpentine elongation achieved for 80 μm thick Cu and superelastic TiNiCuCo serpentines with varying widths. **b** Non-uniform strain distribution of a Cu and TiNiCuCo serpentine (t/w = 80/25) after serpentine elongations of 13 and 32%, respectively. Experiment and FEA comparison of force vs serpentine elongation for a TiNiCuCo serpentine with **c** t/w = 60/75 and **d** t/w = 20/75

phase transformation, implying the maximum principal strain in the material was below $\varepsilon = 1.8\%$.

FEA simulations were implemented to study the change in superelastic behavior for serpentines of different widths and thicknesses. Figure 5a shows simulation results of all t/w ratios for the maximum force from which the superelastic TiNiCuCo serpentines can superelastically recover elongation with no plastic deformation. As the cross-sectional area of the serpentine interconnects increases, there is more SMA material available to actively transform from austenite to stress-induced martensite, thus larger forces can be superelastically recovered. Figure 5b shows the overlay of FEA results and tensile testing experiments until sample fracture for 20 μm thick TiNiCuCo serpentines. Even though the model neglects out-of-plane movement, these experiments verify that the FEA model

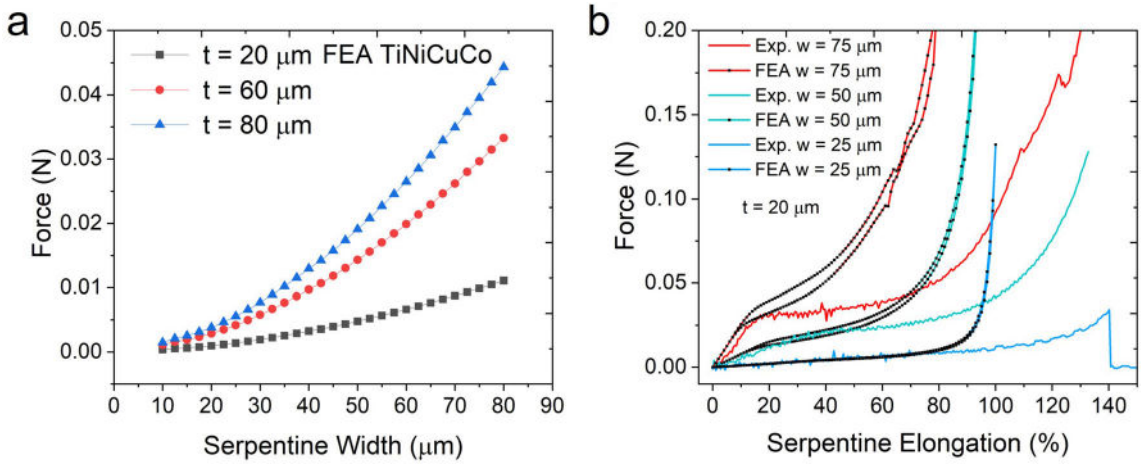

Fig. 5 **a** FEA prediction of maximum critical force that results in superelastic deformation for all t/w aspect ratios. **b** FEA and experiment comparison of maximum serpentine elongation before fracture for serpentines with t/w = 20/25, 20/50, and 20/75

was able to accurately predict the critical force value for serpentines that were experimentally shown to undergo out-of-plane buckling deformation, as shown in Fig. 2c.

Figure 6a shows FEA results for the von Mises stress distribution, first principal strain, and martensitic volume fraction distributions along a TiNiCuCo serpentine (t/w = 80/50) after applying a serpentine elongation of 50%. The non-uniform strain distribution along the serpentine causes the maximum stress/ strain to concentrate along the serpentine's inner arc which is the location of the maximum radius of curvature. After a serpentine elongation of 50%, FEA results predict a maximum principal strain of $\varepsilon = 6\%$ in the inner arc of the serpentine which are the corresponding regions where the superelastic material is transforming from austenite to stress-induced martensite. The inner arcs are the location of built-up remnant martensite that led to minor plastic deformation in the superelastic serpentine.

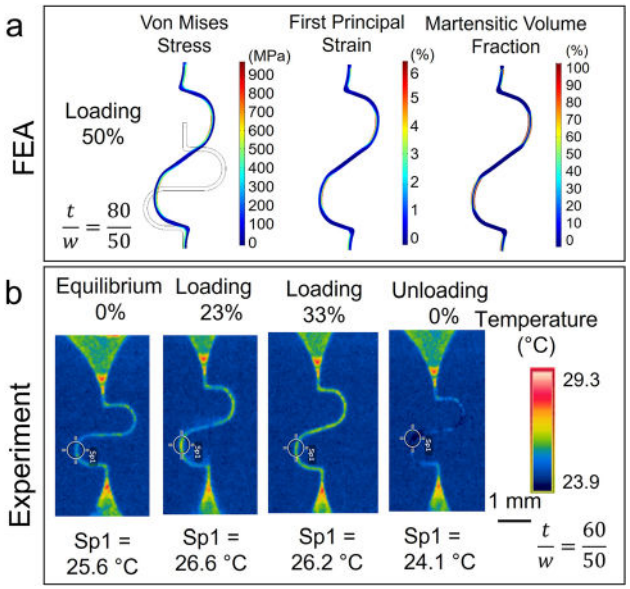

Fig. 6 **a** FEA simulations of the von Mises stress, first principal strain, and martensitic volume fraction distribution of a TiNiCuCo serpentine (t/w = 80/50) after a serpentine elongation of 50%. **b** IR imaging demonstrating the elastocaloric effect in a superelastic TiNiCuCo serpentine (t/w = 60/50) during loading and unloading between 0 and 33% serpentine elongation

Another advantage of using the alloy TiNiCuCo for stretchable electronics is that previously it was identified to be an excellent elastocaloric material [44, 48, 52–55]. The elastocaloric effect results in the heating/ cooling of SMA materials during superelastic strain loading/ unloading. When the SMA undergoes the phase transformation from austenite to stress-induced martensite, the release of latent heat results in an increase in temperature locally on the sample [48]. An infrared (IR) camera can be used to verify regions of maximum strain concentration by determining the localized regions along the serpentine that undergo maximum temperature change. This principle was used to confirm the FEA results, by experimentally strain testing a serpentine with t/w = 60/50 under an IR camera. These results can be compared to the FEA stress/ strain distribution results for the serpentines with t/w = 80/50, since both samples were shown to undergo in-plane scissoring stretching behavior. As shown in Figure 6b, during strain loading between serpentine elongations of 0 and 23%, the temperature of the arc of the serpentine increased from a starting temperature of 25.6 to 26.6 °C. Upon further strain loading to elongations of 33%, the latent heat was distributed throughout the entire serpentine structure. Thus, the temperature in the serpentine arc slightly decreased from 26.6 °C to 26.2 °C. During unloading, the temperature of the arc of the serpentine decreased from 26.2 °C to below 24.1 °C, confirming the reverse transformation from stress-induced martensite to austenite. Figure 7 shows

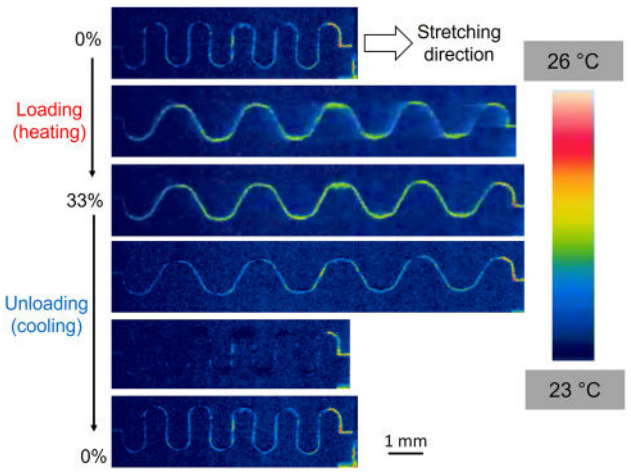

Fig. 7 IR imaging results visualizing regions of maximum strain concentration via the regions of maximum temperature change during strain loading and unloading

similar IR imaging results on a five-period serpentine (t/w = 60/50) after a 33% serpentine elongation, confirming localized temperature change at the arcs of adjacent serpentines. These results validate the FEA results of localized strain concentration in the inner arc of the serpentine which is in alignment with previous serpentine mechanics studies [15, 18, 56, 57].

Stretchable Electrical Resistance Testing

The stress-induced phase transformation was detected by monitoring the electrical resistance of TiNiCuCo serpentines with a four-point probe measurement setup while loading and unloading serpentine elongations between 0 and 50% for one cycle. The average change in resistance as a function of serpentine elongation for cycles 1 and 1000 are plotted for serpentines with t/w = 20/50, 20/50, and 20/75 in Fig. 8a. Where provided, the error bars represent the standard deviation from the average value for three tested serpentines for each t/w aspect ratio. In the first stretching cycle between 0 and 50%, there was a small change in the average electrical resistance of 0.53–0.8% for all tested samples. In comparison, 45 μm thick Cu serpentines were reported to have a resistance of 0.4 Ω, which changed by a few percent during stretching [40]. The influence of functional fatigue on the electrical properties of the serpentines was tested by loading and unloading the samples to serpentine elongations between 0 and 30% for 1000 cycles at a strain rate of 0.5 mm/s. After 1000 cycles, there was an overall increase in electrical resistance of only 1% for a sample with t/w = 20/25, implying that this serpentine was stretched within its elastic limit (ε = 1.8%), experiencing very little functional fatigue. However, after stretching 1000 cycles, serpentines with t/w = 20/50 and 20/75 displayed an average increase in electrical resistance of 5 and 19%, respectively. The change in resistance is likely due to the formation of remnant martensite during cycling due to exceeding the reversible transformation strain of the superelastic material.

Here we consider metallic thin-film superelastic serpentines as freestanding wires for circuits and as substrates for other thin-films for stretchable electronics. Five-period TiNiCuCo serpentine mechanical test structures of two different thicknesses (t/w = 20/75, and 80/75) were coated with a 500 nm Cu on one side of the sample and 5 μm Cu on the other side. We show in a proof-of-concept demonstration that these freestanding Cu/TiNiCuCo/Cu serpentine composites can serve as stretchable electrical interconnects using them in a circuit powering two light-emitting diodes (LEDs). The electrical resistance was monitored for a circuit consisting of a power supply, wires, and a Cu/TiNiCuCo/Cu specimen soldered between the two LEDs, as described in detail in the experimental methods. The circuit diagram of the experiment is shown in Fig. 8b.

The electrical resistance of the circuit was monitored while stretching a Cu/TiNiCuCo/Cu freestanding electrical interconnect at serpentine elongations between 0 and 45% ± 5% for 40 cycles. There was no noticeable change in the electrical resistance and performance of the circuit with stretching. This independence of the conductivity under stretching was demonstrated by all tested Cu/TiNiCuCo/Cu serpentine composites, regardless of the SMA substrate thickness. The electrical resistivity of the austenite phase of TiNiCuCo was determined to be 5.43×10^{-7} Ω m, which is higher than that reported for Cu thin-films (1.87×10^{-8} Ω m [38]). Because NiTi-based SMA thin-films have a relatively high resistivity and form a natural, insulative TiO_2 layer, it is likely that the lower resistance in the Cu thin-film coating provides substantially all the electrical conductivity across the specimen.

There was no appreciable change in the circuit when the experiment was repeated for 40 cycles for both the t/w = 20/75 and t/w = 80/75 samples. After the 40th cycle, the Cu/TiNiCuCo/Cu composite's maximum applied serpentine strain was determined. Figure 8b shows the Cu/TiNiCuCo/Cu serpentine composite with a t/w = 20/75 under a strain resulting in a 122% elongation and the serpentine composite with t/w = 80/75 under a strain resulting in a 61% elongation. There was no appreciable change in the circuit resistance when stretching the serpentine to the maximum elongation up to fracture. Overall, the maximum serpentine elongation of the Cu/TiNiCuCo/Cu composite is lower than that of pure TiNiCuCo serpentines shown in Fig. 2a. Freestanding interconnects based on Cu/TiNiCuCo/Cu serpentine composites combine the mechanical

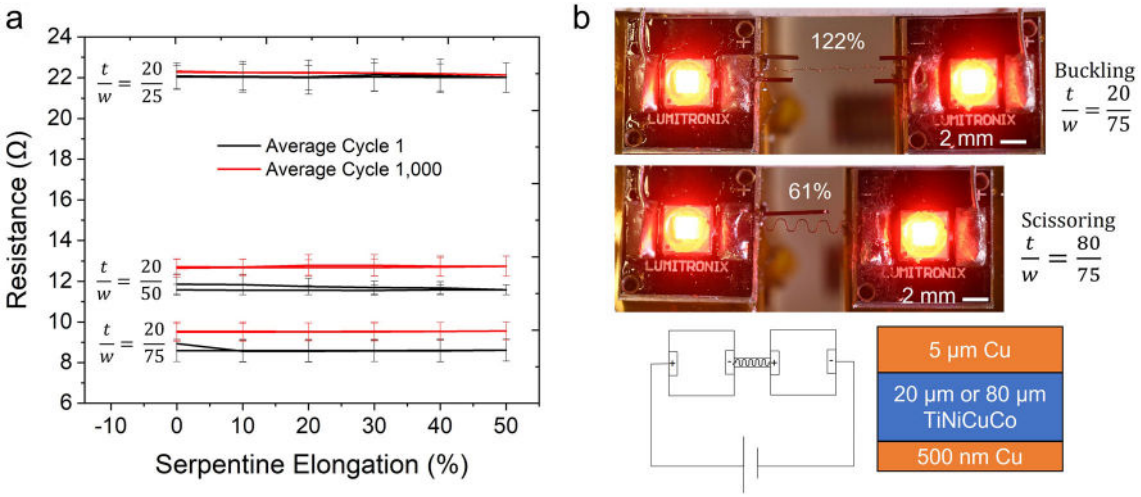

Fig. 8 **a** Strain-dependent electrical resistance measurements at cycle 1 and cycle 1000 for TiNiCuCo serpentines with t/w = 20/25, 20/50, and 20/75. **b** Demonstration of Cu/TiNiCuCo/Cu serpentine composites (TiNiCuCo t/w = 20/75 and 80/75) serving as a stretchable freestanding electrical interconnection between two LEDs

advantages of superelastic films with the electrical advantages of Cu thin-films.

Functional Fatigue Characterization

Slight functional fatigue was observed when cycling all single serpentine mechanical test structures for 200 cycles. Functional fatigue arises due to the accumulation of transformation-induced defects into the microstructure and is reflected by a decrease in the critical stress (and thus critical force) with an increase in cycle number [58]. A representative 'force vs serpentine elongation' curve displaying functional fatigue in a fabricated TiNiCuCo serpentine sample with t/w = 60/50 is shown in Fig. 9a. A serpentine elongation to 50% was superelastically recovered for the first cycle and correlates well with the FEA result. However, after 200 cycles, there was an accumulation of 5.4% unrecovered serpentine elongation.

Ti-rich TiNiCuCo alloys have been reported to have high functional stability but poor structural fatigue life because of the brittleness of the film [55]. Structural fatigue in SMA thin-films can be improved by electropolishing the film's surface because it creates a more homogeneous stress distribution at the edges, and allows for longer cycling lifetimes of up to 10^7 cycles with only negligible functional fatigue [58]. Electropolishing is used to improve the structural fatigue of SMA films by removing small surface defects like scratches, pores, and notches that can cause microcracks in the SMA films [58]. A serpentine with t/w = 60/50 was electropolished, resulting in a

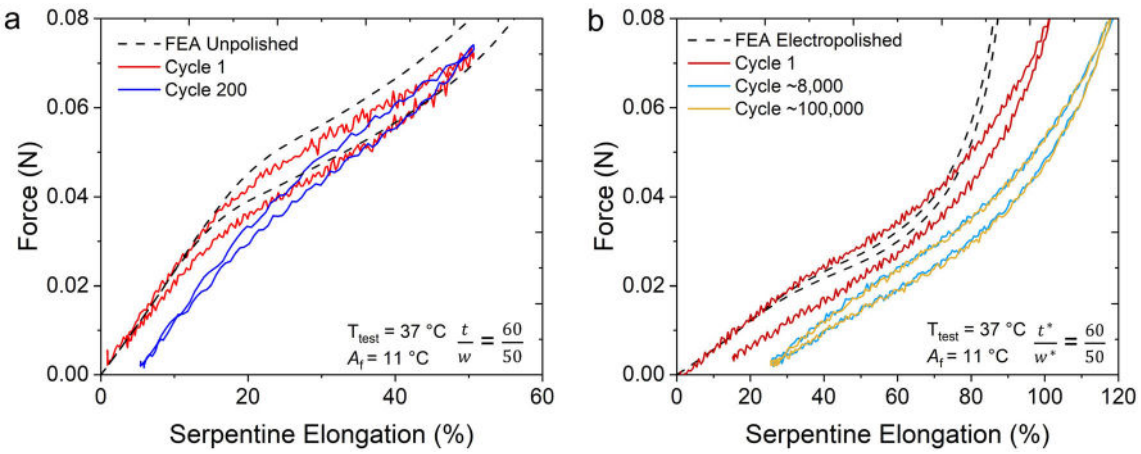

Fig. 9 **a** Degradation in hysteresis loop with superelastic cycling for an unpolished serpentine (t/w = 60/50) after serpentine elongations between 0 and 50% for 200 cycles. **b** Fatigue tensile testing results of an electropolished serpentine (t*/w* = 60/50 before electropolishing) after cycling serpentine elongations of 20–50% at 20 Hz for 100,000 cycles

reduction of the serpentine's width and thickness by a few microns. The reduction in material width and thickness is reflected in the corresponding FEA model. The reduction of the material allows the serpentine to become more flexible, and able to reach larger serpentine elongations at lower critical forces.

Figure 9b shows fatigue testing results for an electropolished serpentine (t*/w* = 60/50 before electropolishing). Force vs serpentine elongation curves were assembled for the sample at elongations between 0 and 100% using the tensile testing methods described in the experimental methods section**.** After 200 cycles, there was only 1.89% of unrecoverable elongation in the serpentine. Fatigue testing then took place in room temperature air at a strain rate of 20 Hz using a custom-built fatigue setup, as described in ref [51]. Serpentines were cycled at serpentine elongations between 20 and 50% at a rate of 20 Hz for 100,000 cycles. Force vs serpentine elongation was again measured displaying a stable hysteresis between cycle numbers ~8000 and ~100,000. The superelastic recovery of extremely large deformations and the stability in the mechanical hysteresis between cycles 8000 and 100,000 show the promise of integrating SMAs into high-life-cycle stretchable electronic applications.

Discussion

The advantageous material properties of sputtered thin-film TiNiCuCo superelastic alloys for stretchable electronics were highlighted in this manuscript. The superelastic effect paired with the serpentine geometries resulted in highly stretchable interconnects. During stretching experiments, all TiNiCuCo samples with a small cross-sectional width (t/w = 20/25, 60/25, and 80/25) reached elongations of 153% ± 4%, approaching the shape of a straight wire. After the sample reached its maximum serpentine elongation and fractured, the serpentines returned to their original shape with minimal plastic deformation, showing the superelastic effect is reversible. In-plane and out-of-plane serpentine deformation was found to be determined by the serpentine's thickness/width aspect ratio, following a similar dependency as reported in prior studies on serpentine mechanics [40].

Experiments and FEA numerical studies on a $Ti_{53.3}Ni_{30.9}Cu_{12.9}Co_{2.9}$ alloy demonstrate the superelastic effect allows recovery of intrinsic elastic strains of ε = 1.8%, which is much larger than Cu thin-films ε = 0.26%. FEA analysis demonstrates the maximum quasi-elastic elongation of thin-film TiNiCuCo serpentines is ~5X–7X larger than that of thin-film Cu serpentines. This significant result suggests it would be advantageous to replace Cu serpentine interconnects with superelastic serpentine interconnects in applications where the stretchable circuit is subjected to large applied deformations because smaller serpentine wavelengths and amplitudes are required to achieve a desired elastic serpentine elongation. FEA analysis also revealed that only a small volume fraction of the TiNiCuCo material transforms from austenite to stress-induced martensite because localized regions (e.g., at the arcs) of the structure undergo significant strain during stretching. The regions predicted by FEA to experience maximum strain concentration were experimentally verified by detecting the elastocaloric effect through IR imaging experiments. The arcs of the serpentine were shown to increase in temperature by 1 °C during strain loading and decrease by 2.1 °C during unloading.

Stretchable bioelectronics ideally requires direct and conformal contact interface with the skin and, should maintain a constant electrical resistance while stretching. All tested freestanding TiNiCuCo samples were shown to have low electrical resistances (9 Ω–22 Ω) which increased by less than 1% when elongating the serpentines between 0 and 50%. Fatigue in the superelastic interconnect was also observed by monitoring the change in electrical resistance with applied cycles. Fatigue in the serpentine can be improved by electropolishing the SMA [58], or by selecting a composition of an SMA that is known to be ultra-low fatigue [36] (i.e., $Ti_{54.7}Ni_{30.7}Cu_{12.3}Co_{2.3}$, $Ti_{54}Ni_{34}Cu_{12}$) and optimizing the microstructure [45] to ensure compatibility between the crystal lattices of the austenite and martensite phases [47]. While the functional fatigue properties of TiNiCuCo are better than that of binary NiTi, TiNiCuCo was found to have intrinsic elastic strains of ε = 1.8%, which is considerably lower than the elastic strains of ε = 7.5% achieved by NiTi [37].

Typical metallic serpentine conductors like Au and Cu cannot be supported in freestanding form, and therefore must be integrated onto a polymeric substrate. SMAs, however, are strong and self-supporting, thus no elastomer is required to provide support or restore force to SMA serpentine structures. Freestanding TiNiCuCo serpentines were demonstrated to serve as substrates for sputter-deposited Cu thin-films. Cu/TiNiCuCo/Cu serpentine composites were demonstrated as freestanding stretchable electrical interconnects between two LEDs. These results support the use of structured freestanding SMAs as substrates to integrate other sputtered materials systems into stretchable electronics. If used as a substrate for stretchable devices in an "island plus serpentine" design, the greater ductility offered by SMA substrates would allow the islands, on which the sensitive components are housed, to remain largely strain-free for longer. Additionally, since SMAs need to be crystallized at temperatures above 400 °C, they could serve as the substrate to enable stretchability within MEMS materials that require high-temperature processing (e.g., semiconductors, piezoelectric

devices) [59]. The excellent mechanical and electric properties of thin-film NiTi-based SMAs make them promising materials to use as interconnects and functional substrates for future wearable and implantable electronics.

Summary and Conclusions

Wearable electronics and implantable medical devices require stretchable circuits which could be based on conductive serpentine structures. The results reported here demonstrate the mechanical advantages of replacing thin-film serpentine interconnects made from traditional metals like Cu with shape memory alloys such as TiNiCuCo. Since the martensitic transformation temperatures are below room temperature, all fabricated TiNiCuCo films demonstrate superelasticity at room temperature. Superelasticity is advantageous for stretchable interconnects because the interconnect will recover from the deformation after the removal of the applied force. FEA simulations reveal elastic serpentine elongations are significantly larger for TiNiCuCo thin-films as compared to Cu thin-films, which is attributed to the increase in intrinsic elastic strain characterized by the superelastic phase transformation in the SMAs. FEA simulations were experimentally verified by tensile testing as well as by detecting temperature changes within the regions of maximum strain concentration for a TiNiCuCo serpentine using infrared imaging.

Cu/TiNiCuCo/Cu serpentine composites were demonstrated to have a stable electrical resistance when stretching between serpentine elongations 0–45% which allowed them to serve as freestanding electrical interconnects between two LEDs. All 20 μm thick TiNiCuCo serpentine interconnects were shown to have low electrical resistances (9 Ω–22 Ω) which increased by less than 1% when elongated between 0 and 50%. The change in resistance was also used to monitor functional fatigue in the serpentine interconnects. Our results show electropolishing as a technique that can be used to improve the mechanical performance of thin-film SMA serpentines, as demonstrated by a stable hysteresis loop between cycle numbers $\sim$8000 and $\sim$100,000 for an electropolished TiNiCuCo serpentine. Since TiNiCuCo is an ultralow-fatigue material, the SMA can theoretically undergo this transformation reversibly for up to 20 million cycles with proper control over the composition and microstructure. These results show the advantage of using sputtered thin-film SMAs as both freestanding substrates and serpentine interconnects in the design of future stretchable electronics.

Acknowledgments This work was supported by the German Research Foundation (Deutsche Forschungsgemeinschaft, DFG) through the special priority program KOMMMA (SPP 2206 - Cooperative Multistage Multistable Microactuator Systems). This material is based upon work supported by the National Science Foundation Graduate Research Fellowship Program under Grant No. DGE 1840340. Any opinions, findings, conclusions, or recommendations expressed in this material are those of the author(s) and do not necessarily reflect the views of the National Science Foundation. The authors thank Dr.-Ing. Prasanth Velvaluri (Kiel University) for assistance with sample fabrication, and Prof. Ichiro Takeuchi (University of Maryland) for discussions regarding the IR imaging experiments.

Funding Open Access funding enabled and organized by Projekt DEAL.

Data availability Data available on request from the authors.

References

1. Kim DH, Ghaffari R, Lu N, Rogers JA (2012) Flexible and stretchable electronics for biointegrated devices. Annu Rev Biomed Eng 14:113–128. https://doi.org/10.1146/annurev-bioeng-071811-150018
2. Kim DH, Lu N, Ma R et al (2011) Epidermal Electronics. Science 333:838–843. https://doi.org/10.1126/science.1206157
3. Xu S, Zhang Y, Cho J et al (2013) Stretchable batteries with self-similar serpentine interconnects and integrated wireless recharging systems. Nat Commun 4:1543. https://doi.org/10.1038/ncomms2553
4. Chortos A, Liu J, Bao Z (2016) Pursuing prosthetic electronic skin. Nat mater 15(9):937–950
5. Wang Y, Li Z, Xiao J (2016) Stretchable thin film materials: fabrication, application, and mechanics. J Electron Packag. https://doi.org/10.1115/1.4032984
6. Rogers JA, Someya T, Huang Y (2010) Materials and mechanics for stretchable electronics. Science 327(5973):1603–1607
7. Rogers JA, Huang Y (2009) A curvy, stretchy future for electronics. Proc Natl Acad Sci. https://doi.org/10.1073/pnas.0905723106
8. Lu N, Yang S (2015) Mechanics for stretchable sensors. Curr Opin Solid State Mater Sci 19:149–159. https://doi.org/10.1016/j.cossms.2014.12.007
9. Widlund T, Yang S, Hsu Y-Y, Lu N (2014) Stretchability and compliance of freestanding serpentine-shaped ribbons. Int J Solids Struct 51:4026–4037. https://doi.org/10.1016/J.IJSOLSTR.2014.07.025
10. Fan Z, Zhang Y, Ma Q et al (2016) A finite deformation model of planar serpentine interconnects for stretchable electronics. Int J

Solids Struct 91:46–54. https://doi.org/10.1016/j.ijsolstr.2016.04.030
11. Gonzalez M, Axisa F, Vanden Bulcke M et al (2008) Design of metal interconnects for stretchable electronic circuits. Microelectron Reliab 48:825–832. https://doi.org/10.1016/j.microrel.2008.03.025
12. Zhang Y, Xu S, Fu H et al (2013) Buckling in serpentine microstructures and applications in elastomer-supported ultrastretchable electronics with high areal coverage. Soft Matter 9:8062. https://doi.org/10.1039/c3sm51360b
13. Hayes GJ, So JH, Qusba A et al (2012) Flexible liquid metal alloy (EGaIn) microstrip patch antenna. IEEE trans Antennas Propag 60(5):2151–2156
14. Gray DS, Tien J, Chen CS (2004) High-conductivity elastomeric electronics. Adv Mater 16:393–397. https://doi.org/10.1002/adma.200306107
15. Pan T, Pharr M, Ma Y et al (2017) Experimental and theoretical studies of serpentine interconnects on ultrathin elastomers for stretchable electronics. Adv Funct Mater. https://doi.org/10.1002/adfm.201702589
16. Lazarus N, Meyer CD, Bedair SS (2015) Stretchable inductor design. IEEE Trans Electron Devices 62:1–1. https://doi.org/10.1109/TED.2015.2431221
17. Zhang Y, Wang S, Li X et al (2014) Experimental and theoretical studies of serpentine microstructures bonded to prestrained elastomers for stretchable electronics. Adv Funct Mater 24(14):2028–2037
18. Curtis SM, Tompkins RP, Nichols BM et al (2019) Structural anisotropy in stretchable silicon. Adv Electron Mater 5(7):1900003
19. Xue Z, Dong T, Zhu Z et al (2018) Engineering in-plane silicon nanowire springs for highly stretchable electronics. J Semicond 39:011001. https://doi.org/10.1088/1674-4926/39/1/011001
20. Fan JA, Yeo W-H, Su Y et al (2014) Fractal design concepts for stretchable electronics. Nat commun 5(1):1–8
21. Kim D-H, Liu Z, Kim Y-S et al (2009) Optimized structural designs for stretchable silicon integrated circuits. Small 5(24):2841–2847
22. Mahaboob I, Marini J, Hogan K et al (2018) Selective area epitaxial growth of stretchable geometry AlGaN–GaN heterostructures. J Electron Mater 47(11):6625–6634
23. Tompkins RP, Mahaboob I, Shahedipour-Sandvik F, Lazarus N (2017) Electrical properties of AlGaN/GaN HEMTs in stretchable geometries. Solid-State Electron 136:36–42
24. Sharma N, Raj T, Jangra K (2015) Applications of nickel-titanium alloy. J Eng Technol 5(1):1
25. Jani JM, Leary M, Subic A, Gibson MA (2014) A review of shape memory alloy research, applications and opportunities. Mater Design 1980–2015(56):1078–1113
26. Bechtold C, de Miranda RL, Chluba C, Quandt E (2016) Fabrication of self-expandable NiTi thin film devices with microelectrode array for bioelectric sensing, stimulation and ablation. Biomed microdevices 18(6):106
27. Kohl M, Dittmann D, Quandt E, Winzek B (2000) Thin film shape memory microvalves with adjustable operation temperature. Sens Actuators A: Phys 83(1–3):214–219
28. Miyazaki S, Fu YQ, Huang WM (2009) Thin film shape memory alloys: fundamentals and device applications. Cambridge University Press, Cambridge
29. Bechtold C, Chluba C, Zamponi C et al (2019) Fabrication and characterization of freestanding NiTi based thin film materials for shape memory micro-actuator applications. Shape Mem Superelasticity 5(4):327–335
30. Kohl M (2004) Shape memory microactuators. Springer Science & Business Media, Berlin
31. Curtis SM, Sielenkämper M, Arivanandhan G et al (2022) TiNiHf/SiO2/Si shape memory film composites for Bi-directional micro actuation. Int J Smart Nano Mater 13(2):293–394. https://doi.org/10.1080/19475411.2022.2071352
32. Choudhary N, Kaur D (2016) Shape memory alloy thin films and heterostructures for MEMS applications: a review. Sens Actuators A: Phys 242:162–181
33. Fu Y, Du H, Huang W et al (2004) TiNi-based thin films in MEMS applications: a review. Sens Actuators A: Phys 112(2–3):395–408
34. Otsuka K, Ren X (2005) Physical metallurgy of Ti–Ni-based shape memory alloys. Progress mater sci 50(5):511–678
35. Bumke L, Zamponi C, Jetter J, Quandt E (2020) Cu-Rich Ti52.8Ni22. 2Cu22. 5Co2. 5 shape memory alloy films with ultra-low fatigue for elastocaloric applications. J Appl Phys 127(22):225105
36. Chluba C, Ge W, de Miranda RL et al (2015) Ultralow-fatigue shape memory alloy films. Science 348(6238):1004–1007
37. Zhao Y, Zhou W, Shi Y et al (2022) Superelastic alloy based electrical interconnects for highly stretchable electronics. npj Flex Electron 6(1):1–8
38. Mech K, Kowalik R, Żabiński P (2011) Cu thin films deposited by DC magnetron sputtering for contact surfaces on electronic components. Arch Metall mater 56(4):903–908
39. Pan C, Kumar K, Li J et al (2018) Visually imperceptible liquid-metal circuits for transparent, stretchable electronics with direct laser writing. Adv Mater 30(12):1706937
40. Su Y, Ping X, Yu KJ et al (2017) In-plane deformation mechanics for highly stretchable electronics. Adv Mater 29(8):1604989
41. Lima de Miranda R, Zamponi C, Quandt E (2013) Micropatterned freestanding superelastic TiNi films. Adv Eng Mater 15(1–2):66
42. Bechtold C, de Miranda RL, Quandt E (2015) Capability of sputtered micro-patterned NiTi thick films. Shape Memory Superelastic 1:286–293. https://doi.org/10.1007/s40830-015-0029-9
43. Curtis SM, Dengiz D, Bumke L, Quandt E (2022) Auxetic Superelastic TiNiCuCo Sputtered Thin-Films For Stretchable Electronics. In: SMST2022. pp 11–13
44. Bruederlin F, Ossmer H, Wendler F et al (2017) SMA foil-based elastocaloric cooling: from material behavior to device engineering. J Phys D: Appl Phys 50(42):424003
45. Chluba C, Ge W, Dankwort T et al (2016) Effect of crystallographic compatibility and grain size on the functional fatigue of sputtered TiNiCuCo thin films. Philos Trans Royal Soc A: Math, Phys Eng Sci 374(2074):20150311
46. Cui J, Chu YS, Famodu OO et al (2006) Combinatorial search of thermoelastic shape-memory alloys with extremely small hysteresis width. Nat mater 5(4):286–290
47. Gu H, Bumke L, Chluba C et al (2018) Phase engineering and supercompatibility of shape memory alloys. Mater Today 21(3):265–277
48. Ossmer H, Chluba C, Gueltig M et al (2015) Local evolution of the elastocaloric effect in TiNi-based films. Shape Memory Superelastic 1(2):142–152
49. Morgiel J, Cesari E, Pons J et al (2002) Microstructure and martensite transformation in aged Ti-25Ni-25Cu shape memory melt spun ribbons. J mater sci 37(24):5319–5325
50. Lv C, Yu H, Jiang H (2014) Archimedean spiral design for extremely stretchable interconnects. Extreme Mech Lett 1:29–34
51. Gugat JL, Bechtold C, Chluba C et al (2020) High-cycle mechanical fatigue performance of sputtered nitinol. J Mater Eng Perform 29(3):1892–1900
52. Ossmer H, Chluba C, Kauffmann-Weiss S et al (2016) TiNi-based films for elastocaloric microcooling—fatigue life and device performance. APL Mater 4(6):64102

53. Chluba C, Ossmer H, Zamponi C et al (2016) Ultra-low fatigue quaternary TiNi-based films for elastocaloric cooling. Shap Mem Superelasticity 2(1):95–103
54. Bumke L, Chluba C, Ossmer H et al (2018) Cobalt gradient evolution in sputtered TiNiCuCo films for elastocaloric cooling. Physica status solidi (b) 255(2):1700299
55. Bruederlin F, Bumke L, Chluba C et al (2018) Elastocaloric cooling on the miniature scale: a review on materials and device engineering. Energ Technol 6(8):1588–1604
56. Lazarus N, Meyer CD, Bedair SS et al (2015) Magnetic elastomers for stretchable inductors. ACS Appl Mater Interf 7:10080–10084. https://doi.org/10.1021/acsami.5b02189
57. Zhang Y, Wang S, Li X et al (2013) Experimental and theoretical studies of serpentine microstructures bonded to prestrained elastomers for stretchable electronics. Adv Funct Mater 24(14):2028–2037
58. Frenzel J (2020) On the importance of structural and functional fatigue in shape memory technology. Shap Mem Superelasticity 6(2):213–222
59. Curtis SM, Wolff N, Dengiz D et al (2020) Integration of AlN piezoelectric thin films on ultralow fatigue TiNiCu shape memory alloys. J Mater Res 35(10):1298–1306. https://doi.org/10.1557/jmr.2020.106